AMERICAN SCIENTIFIC PUBLISHERS

Journal of
Nanoscience and Nanotechnology
Vol. 15, 1–17, 2015
www.aspbs.com/jnn

Aloe vera Plant Extracted Green Synthesis, Structural and Opto-Magnetic Characterizations of Spinel $Co_xZn_{1-x}Al_2O_4$ Nano-Catalysts

A. Manikandan[1,*], M. Durka[2], M. Amutha Selvi[3], and S. Arul Antony[1,*]

[1] *PG and Research Department of Chemistry, Presidency College (Autonomous), Chennai 600005, India*
[2] *Department of Physics, A.V.V.M Sri Pushpam College (Autonomous), Poondi, Thanjavur 613503, Tamil Nadu, India*
[3] *Department of Chemistry, Avinashilingam Institute for Home Science and Higher Education for Women University, Coimbatore 641043, India*

Spinel $Co_xZn_{1-x}Al_2O_4$ ($0 \leq x \leq 1$) nano-catalysts were synthesized by a simple *Aloe vera* plant extracted green synthesis route. Powder XRD patterns and Rietveld analysis confirmed the formation of single phase, cubic spinel gahnite structure without other impurities. The lattice parameter increased from 8.089 to 8.125 Å with increasing Co^{2+} content. The average crystallite sizes were estimated using Scherrer's method, and it was found to be in the range of 15.72 nm to 26.53 nm. FT-IR spectra showed vibrational stretching frequencies corresponding to the spinel structure. HR-SEM and HR-TEM images showed the features of well particle shaped crystals with nano-sized grains. The elemental compositions of Co, Zn, Al and O were quantitatively obtained from EDX analysis. The band gap energy estimated using Kubelka-Munk method by UV-Visible DRS method, and the values are decreased with increasing the Co^{2+} content (4.12 eV to 3.67 eV), due to the formation of sub bands in between the energy gap. PL spectra showed emission bands in UV as well as in the visible regions for $ZnAl_2O_4$ and Co-doped $ZnAl_2O_4$, due to the defect centers acting as the trap levels. VSM measurements revealed that pure $ZnAl_2O_4$ has diamagnetic, while Co doped $ZnAl_2O_4$ samples ($x = 0.2$ to 0.8) have superparamagnetism, whereas the sample $CoAl_2O_4$ has ferromagnetic in nature. Catalytic oxidation of benzyl alcohol to benzaldehyde was found that the sample $Co_{0.6}Zn_{0.4}Al_2O_4$ showed 93.25% conversion with 99.56% selectivity, whereas for pure $ZnAl_2O_4$, the conversion was only 86.31% with 92.85% selectivity.

Keywords: Spinel $ZnAl_2O_4$, Plant Extract, Nano-Crystals, Optical Properties, Magnetic Properties, Catalytic Properties.

1. INTRODUCTION

Nanocrystalline spinels are a class of binary transition metal oxide semiconductors signify an attractive materials, which owing to their small size; exhibits novel physicochemical properties.[1,2] According to the distribution of cations in tetrahedral (A-) and octahedral (B-) sites, spinels are classified into normal and inverse structure. In normal spinel, the divalent (A^{2+}) cations on A-sites and the trivalent (B^{3+}) cations on B-sites, and is represented by the formula $^{IV}(A^{2+})^{VI}(B^{3+}B^{3+})O_4$. However, the inverse spinel, with the formula $^{IV}(B^{3+})^{VI}(A^{2+}B^{3+})O_4$, in which the divalent cations occupy the B-sites and the trivalent cations are equally divided among A- and B-sites, where, A and B represents the divalent (Co^{2+}, Ni^{2+}, Cu^{2+}, Zn^{2+}, etc.) and trivalent (Fe^{3+}, Al^{3+}, etc.) cations occupying A- and B-sites, respectively, of a cubic crystal structure with a space group Fd-3m.[3,4]

Among various binary transition metal oxides, zinc aluminate ($ZnAl_2O_4$), has gained lot of interest in multidisciplinary areas, due to their effectiveness in ceramics, electronic, optical, catalyst, catalyst supports, aerospace, paints, dielectrics and sensing applications.[2–5] Spinel $ZnAl_2O_4$ is a direct wide band gap semiconductor with optical band gap value of about 3.8 eV and may find applications in optoelectronic devices operated in the ultraviolet region. Spinel $ZnAl_2O_4$ offers many beneficial properties

*Authors to whom correspondence should be addressed.

such as high mechanical strength, high thermal stability, low surface acidity, and better diffusion, low temperature sintering ability, high chemical stability, wide band-gap energy, hydrophobic behavior, excellent optical transparency, good metal dispersion capacity, low surface acidity and high quantum yields.[6, 7] Also, $ZnAl_2O_4$ is a semiconductor suitable for ultraviolet photoelectronic application.[8]

Several methods have been used for the preparation of nanocrystalline $ZnAl_2O_4$ such as hydroxide precursors,[5] microwave assisted hydrothermal,[6] co-precipitation,[9] sol–gel,[10] hydrothermal,[11] polymeric precursors,[12] template assisted,[13] glycothermal,[14] combustion[15] and solid-state reaction[16] methods. However, the above methods need sophisticated equipment and are expensive. The main disadvantages of the high temperature in sol–gel, co-precipitation and other methods are that the products obtained with higher particle size typically possess low surface area and inhomogeneity. Moreover, the above methods claims costly materials that generate toxic organic/inorganic intermediates and laborious synthetic procedures, thus leading to the tedious polluting process. Also, the above methods of preparation procedures were performed for long-time with high temperature.

However, the high surface area with a porous structure of $ZnAl_2O_4$ is of great importance for catalytic activity. Therefore, in the present study, an attempt is given to synthesize single phase and porous $ZnAl_2O_4$ with high specific surface area using *Aloe vera* plant extract by the simple microwave-assisted combustion method (MCM). Recently, a novel method has been developed with the purpose of obtaining nanocrystalline solid materials with porous structure and high surface area, called microwave-assisted combustion method (MCM). In this method the microwave energy interacts with the reactant (*Aloe vera* and metal nitrates) raw materials at the molecular level, and the energy transferred into heat, which is distributed homogeneously through the material interior, results of rapid heating, early phase formation of nanoparticles, faster kinetics and energy saving, leading to a more homogeneous nucleation and a shorter crystallization time than other methods.[17] In this method, the samples are prepared at low temperatures, low cost with good control of size, structure and morphology. Mixed oxides obtained by MCM synthesis are usually nanocrystalline materials with well controlled size, morphology and chemical composition with very interesting textural properties.[18, 19]

Generally, the combustion based preparation method offers one of the most easily reached, fast and low energy soft methods in comparison to the above said methods. As a result, morphology, surface area, crystallite size and other physicochemical properties can be altered. In the present days, citric acid, urea, sucrose, glycine, *b*-alanine, starch, carbohydrazide, *N*-methylurea and hexamethylenetetramine are chosen as fuels for combustion reactions.[20] However, the above fuels can reacts with moisture in humid air to produce a corrosive, toxic and irritating mist, to which even short exposures can cause serious damage to health. Therefore, simple and cost effective routes to synthesize nanocrystalline $ZnAl_2O_4$ by utilization of cheap, nontoxic and environmentally benign precursors are still the key issues.

Aloe vera (*Aloe barbadensis Miller*) is a permanent juicy belonging to the *Liliaceal* family, and it is a cactus-like plant that grows in hot, dry climates.[21] Recently, *Aloe vera* plant extract gelling solution has been used in the preparation other materials such as Au, Ag nanoparticles,[22] MFe_2O_4 (M = Ni, Co, Mn, Mg, Zn) nanostructures,[23] In_2O_3 nanoparticles,[24] (Ni–Cu–Zn)Fe_2O_4 nanostructures.[25] In the modern simple synthetic method using cheap precursors of aloe vera plant extracted gelling solution provides high-yield nanosized materials with well crystalline structure and good opto-magnetic and catalytic properties. Also, the method can be used to prepare nanocrystalline oxides of other interesting materials. The advantages of *Aloe vera* plant extracted MCM route include the use of cheap, nontoxic and environmentally benign precursors, also the procedures are simple, without time-consuming polymerization and problem with treatment of a highly viscous polymeric resin and no need for higher temperature calcinations and costly equipment.

Aluminium based spinel semiconductors represent an interesting class of oxide materials with significant technological applications in interdisciplinary areas. Moreover, no literature precedence, to our knowledge, is available on the synthesis and optical, magnetic and catalytic properties of nano-scaled transition metal aluminates by a simple aloe vera plant extracted MCM route. However, in our present case, the samples were prepared using *Aloe vera* plant extracted MCM route is a green synthesis non-polluting with low cost. Generally, MCM approach is fast, simple, uniform heating, energy efficient and has been widely used by many researchers. Therefore, if such a $ZnAl_2O_4$ with high surface area could be conveniently prepared by MCM route, and the obtained samples would be more attractive for catalytic applications.

Among various nano-metal oxides, spinel-type mixed oxides (AB_2O_4) are well known for their rich catalytic action. Among them, $ZnAl_2O_4$ has been used extensively as a heterogeneous catalyst and it can be recovered easily from the reaction mixture by simple filtration and reused several times, making the process more economically and environmentally viable. These oxides are non-toxic, inexpensive and they have high melting points, relatively high surface areas and these properties make them suitable for use as solid heterogeneous catalysts. Heterogeneous catalytic nano-materials play a very important role in the selective protection of functional groups in ways that are economically advantageous and environmentally friendly. The catalytic property of the nanocrystalline spinel metal oxide semiconductors significantly depends on the distribution of cations among the A- and B-sites of the spinels.

Jacobs et al.[26] established that in spinels, the B-sites are almost exclusively exposed in the crystallites and that the catalytic activity was mainly due to B-cations. Generally, two main factors affecting the catalytic property of catalysts are the specific surface area and porous structure, and typically a high surface area goes along with small particle size, which enhances the catalytic activity. Walerczyk et al.[11] have reported catalytic properties of nano-sized $Zn_{1-x}Co_xAl_2O_4$ ($x = 0$, 0.5, 1.0) spinels and they found that the sample $Co_{0.5}Zn_{0.5}Al_2O_4$ with specific properties with good catalytic performance for phenol methylation to ortho-methylated derivatives. It was acknowledged that $ZnAl_2O_4$ as an active and selective catalyst.[27–30] The researchers reported, that the high active aluminate catalysts, which enable obtaining methylated phenols[27] and efficient methylation of 2- and 4-hydroxypyridine.[28, 29] The catalytic properties in methylation of phenol of $ZnAl_2O_4$ with incorporation of different metals (e.g., Cu) were also investigated.[31] Kapse et al.[32] have reported nanocrystalline $Zn_{1-x}Co_xAl_2O_4$ ($x = 0$, 0.2, 0.4, 0.6, 0.8, 1) spinels prepared by citrate sol–gel method for ethanol gas sensor application. Studies on the optical, magnetic and catalytic properties of spinel $ZnAl_2O_4$ nanoparticles were carried out by many researchers, but there is no reports found in literature for the preparation of this material using *Aloe vera* plant extract solution by MCM. In the present study, we have reported the effect of Co^{2+}-doping on structural, morphological, optical, magnetic and catalytic properties of $ZnAl_2O_4$ nano-crystals prepared by a simple *Aloe vera* plant extracted one-pot MCM route.

2. EXPERIMENTAL PART

2.1. Materials and Methods

All the chemicals used in this study were of analytical grade obtained from Merck, India and were used as received without further purification. All chemicals such as nitrates of zinc, cobalt and aluminum, and *Aloe vera* plant extracted solution as the raw materials were used for this method. Millipore water was used for the entire preparation process of the samples. The *Aloe vera* leaves were collected from the local agricultural fields, Athanur, Peravurani, Thanjavur District 614804, Tamilnadu, India. *Aloe vera* plant extracted solution was prepared from a 5 g portion of thoroughly washed *Aloe vera* leaves were finely cut and the gel obtained was dissolved in 10 ml of de-ionized water and stirred for 30 min to obtain a clear solution. The resulting product was used as an *Aloe vera* plant extracted solution.

In the preparation of $ZnAl_2O_4$ sample, zinc nitrate (5 mmol) and aluminium nitrate (10 mmol) were first dissolved in the *Aloe vera* plant extracted solution under vigorous stirring at room temperature for 1 h until a clear transparent solution was obtained. In this preparation process, *Aloe vera* plant extracted solution has a double function of both reducing and gelling agent for the synthesis of mixed metal oxides (Scheme 1). Metal nitrate salts and *Aloe vera* plant extracted solution were chosen by considering the total reducing and oxidizing agent valences of the raw materials and were quantified in equivalence of NOx reduction (N_2O to N_2, CO_2 and H_2O) at a low temperature. The precursor mixture of metal nitrates in *Aloe vera* extract solution was placed in a domestic microwave oven (SAMSUNG, India Limited) and exposed to the microwave energy in a 2.45 GHz multimode cavity at 850 W for 10 min. Initially, the precursor mixture boiled and underwent evaporation followed by the decomposition with the evolution of gases. When the solution attained the point of spontaneous combustion, ignition took place resulting in a rapid flame and yielding solid fluffy final products of mixed metal oxides. After completion of the reaction, the obtained solid powder was then washed with ethanol and dried at 70 °C for 1 h. The obtained powders were labeled as $ZnAl_2O_4$, $Co_{0.2}Zn_{0.8}Al_2O_4$, $Co_{0.4}Zn_{0.6}Al_2O_4$, $Co_{0.6}Zn_{0.4}Al_2O_4$, $Co_{0.8}Zn_{0.2}Al_2O_4$ and $CoAl_2O_4$, respectively for $x = 0.0$, 0.2, 0.4, 0.6, 0.8 and 1 in $Co_xZn_{1-x}Al_2O_4$ system.

2.2. Characterization Techniques

The structural characterization of spinel $Co_xZn_{1-x}Al_2O_4$ ($x = 0.0$, 0.2, 0.4, 0.6, 0.8 and 1) nano-crystals were performed using a Rigaku Ultima X-ray diffractometer (XRD) for 2θ values ranging from 10 to 80° using Cu-Kα radiation ($\lambda = 1.5418$ Å). Structural refinements using the Rietveld method was carried out using PDXL program; both refined lattice parameters and crystallite size of the obtained powders were reported. The surface functional groups were analyzed by Perkin Elmer FT-IR spectrometer. The surface morphology of the samples was achieved at desired magnification with a Joel JSM 6360 high resolution scanning electron microscope (HR-SEM) equipped with energy dispersive X-ray (EDX) for elemental composition analysis. The transmission electron micrographs were carried out by Philips-TEM (CM20). The UV-Visible diffuse reflectance spectrum (DRS) was recorded using Cary100 UV-Visible spectrophotometer to estimate their band gap. The photoluminescence (PL) properties were recorded using Varian Cary Eclipse Fluorescence Spectrophotometer. Magnetic measurements were carried out

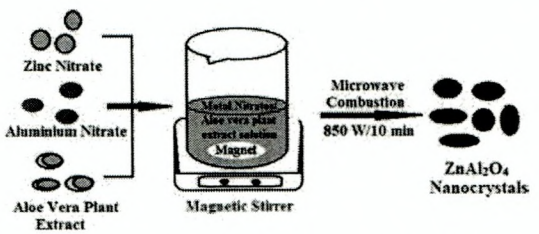

Scheme 1. Schematic diagram of preparation procedure of *Aloe vera* plant extracted MCM synthesis of spinel $Co_xZn_{1-x}Al_2O_4$ ($x = 0.0$, 0.2, 0.4, 0.6, 0.8 and 1) nano-crystals.

at room temperature using a PMC MicroMag 3900 model vibrating sample magnetometer (VSM) equipped with 1 Tesla magnet.

2.3. Catalytic Test

The oxidation of benzyl alcohol using spinel $Co_xZn_{1-x}Al_2O_4$ nano-crystals was carried out in a batch reactor operated under atmospheric conditions. 5 mmol of oxidant (H_2O_2) was added along with 0.5 g of nano-sized spinel $Co_xZn_{1-x}Al_2O_4$ catalysts ($x = 0.0$, 0.2, 0.4, 0.6, 0.8 and 1) and the contents were heated at 80 °C in an acetonitrile medium for 5 h in a three necked round bottom flask equipped with a reflux condenser and thermometer. The oxidized products after the catalytic reaction are collected and studied using Agilent GC spectrometer. The column used for the study was DB wax column (capillary column) of length 30 mm and helium was used as the carrier gas. GC technique was carried out to know the conversion percentage of the products. The yields of benzaldehyde formed were calculated by the following formula (1) and (2),

$$\text{Conversion (\%)} = \frac{\text{Std. peak area} - \text{Sample peak area}}{\text{Sample peak area}} \times 100 \quad (1)$$

$$\text{Selectivity (\%)} = \frac{\text{Sample peak area}}{\text{Total peak area}} \times 100 \quad (2)$$

3. RESULTS AND DISCUSSION

3.1. Structural analysis

Powder X-ray diffraction (XRD) analysis was used to investigate the phase structure and average crystallite size of the spinel $Co_xZn_{1-x}Al_2O_4$ ($x = 0.0$, 0.2, 0.4, 0.6, 0.8 and 1) nanocrystals. Figure 1 shows the typical XRD patterns of spinel $Co_xZn_{1-x}Al_2O_4$ powders obtained at a different concentration of Co^{2+} dopant. The characteristic peaks at 2θ of 31.24, 36.77, 38.72, 44.79, 49.11, 55.78, 59.42, 65.37, 74.29 and 77.56° are corresponding to (220), (311), (222), (400), (331), (422), (511), (440), (620) and (533) diffraction planes. According to the XRD patterns, all diffraction peaks can be perfectly indexed as centered cubic spinel structured $ZnAl_2O_4$ (JCPDS card no. 05-0669)[33] and $CoAl_2O_4$ (JCPDS card no. 38-0814),[1,14] respectively. The intensities and position of the peaks of the synthesized powders are in agreement with those of standard JCPDS and no other peak of any phase was detected, which indicates that the prepared samples were pure crystalline materials.

The average crystallite size calculated from the most intense X-ray diffraction peak (311) using scherrer's Eq. (3),

$$D = \frac{0.89\lambda}{\beta \cos\theta} \quad (3)$$

where 'D' is the crystallite size, 'λ,' the X-ray wavelength, 'θ,' the Bragg diffraction angle and 'β,' the full width

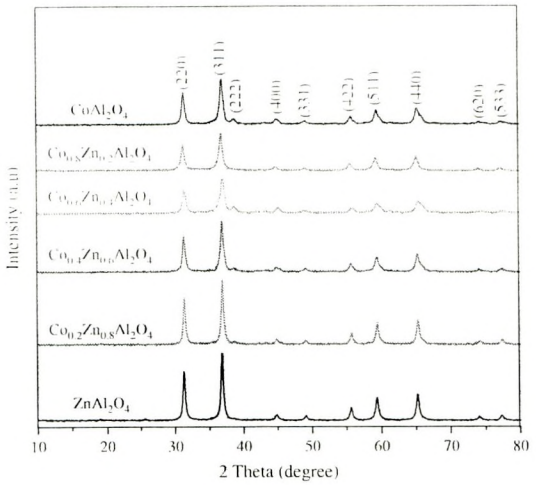

Figure 1. XRD patterns of spinel $Co_xZn_{1-x}Al_2O_4$ ($x = 0.0$, 0.2, 0.4, 0.6, 0.8 and 1) nano-crystals.

at half maximum (FWHM). The average crystallite size was estimated by applying the Scherrer's equation on the peak at $2\theta = 36.77°$ for all samples. The dependence of the average $ZnAl_2O_4$ crystallite sizes on the Co^{2+} doping concentration is shown in the Table I. It was found that the average crystallite size was higher (27.23 nm) for pure $ZnAl_2O_4$ while the crystallite size decreased to 15.72 nm for the Co-doped $ZnAl_2O_4$ ($x = 6$, i.e., $Co_{0.6}Zn_{0.4}Al_2O_4$). The XRD broadening peaks in $Co_xZn_{1-x}Al_2O_4$ samples strongly suggest that Co^{2+} ions were successfully substituted into $ZnAl_2O_4$ host structure. It can be seen that the widths of peaks for the sample obtained at higher concentration of Co-dopant ($Co_{0.6}Zn_{0.4}Al_2O_4$) are broader, indicating that the crystallite size is very small. However, the undoped $ZnAl_2O_4$ sample show sharp peak results higher crystallite size. However, further increase in Co doping, $x = 0.8$ and 1 increased the crystallite size to 17.69 nm and 21.86 nm respectively. The result reveal at lower doping of Co ($x = 0.2$, 0.4 and 0.6) controls and retards the growth of the crystallite size, while higher doping of Co ($x = 0.8$ and 1.0) favors the growth of the crystallite size at the nucleation centers, which resulted higher crystallite size. With increasing the Co^{2+} content, the intensity of the diffraction peaks decreases, which is associated with a decrease in the crystalline size, but the position of the peaks, remain unchanged. The broad diffraction lines of samples indicated that the nano-crystalline nature of the products. However, the effective crystallite size (D) calculated using Scherrer's equation for all the samples is in good agreement with that of the results obtained by Rietveld refinement XRD method as shown in Table I.

The lattice parameter of spinel $Co_xZn_{1-x}Al_2O_4$ ($x = 0.0$, 0.2, 0.4, 0.6, 0.8 and 1) powders was calculated based on the X-ray diffraction patterns using Eq. (4)

$$a = d_{hkl}(h^2 + k^2 + l^2) \quad (4)$$

Table I. Lattice parameter, crystallite size (Scherer formula and Rietveld analysis) and band gap values of spinel $Co_xZn_{1-x}Al_2O_4$ ($x = 0.0$, 0.2, 0.4, 0.6, 0.8 and 1) nano-crystals.

Samples	Crystallite size (nm)		Lattice parameter (Å)		Band gap (eV)	Unit cell volume (Å^3)	Strain (%)	S (goodness of fit)
	Scherrer formula	Rietveld analysis	Calculated values	Rietveld analysis				
$ZnAl_2O_4$	26.53	27	8.088	8.089	4.12	525.64	0.073	1.113
$Co_{0.2}Zn_{0.8}Al_2O_4$	22.67	23	8.091	8.092	3.92	528.39	0.078	1.111
$Co_{0.4}Zn_{0.6}Al_2O_4$	19.58	21	8.096	8.098	3.89	530.04	0.075	1.112
$Co_{0.6}Zn_{0.4}Al_2O_4$	15.72	16	8.103	8.105	3.82	533.25	0.072	1.114
$Co_{0.8}Zn_{0.2}Al_2O_4$	17.69	19	8.115	8.113	3.75	535.47	0.074	1.110
$CoAl_2O_4$	21.86	22	8.125	8.123	3.67	537.76	0.069	1.115

where, 'a' is the lattice constant, 'd_{hkl}' the interplanar spacing corresponding to the Miller indices, '*h,*' '*k,*' *and* '*l*' the miller indices.[34] The calculated values of lattice parameters (lattice constant (a) and unit-cell volume) are summarized in Table I. It was found that the lattice constant (a) is to be affected by the Co^{2+}-dopant stoichiometry. The value of lattice constant, a (8.089 Å) for the $ZnAl_2O_4$ is in good agreement with that reported value (8.088 Å) by Wei and Chen.[35] The lattice parameter almost linearly increased by Co^{2+} content addition, thus obeying Vegard's rule. As the doping concentration of Co^{2+} content increases from $x = 0.2$ to 1.0, the lattice constant increased from 8.091 to 8.125 Å, which are consistent with earlier reported results on Co^{2+} doped spinel $ZnAl_2O_4$ nanostructures by Kapse et al.[32] and Duan et al.[36] Ardit et al. reported that the increase in lattice constant is due to the different covalence degree exerted by the two oxygen coordinated ions i.e., Zn and Co respectively.[37] However, the effectual lattice parameter (a) calculated using the above formula for all the samples is in good agreement with that of the results obtained by Rietveld refinement XRD analysis as shown in Table I.

Rietveld refinement XRD analysis were performed on spinel $Co_xZn_{1-x}Al_2O_4$ ($x = 0.0$, 0.2, 0.4, 0.6, 0.8 and 1) samples using FULLPROF program,[38] to characterize the structural aspect of the materials. Rietveld refinement XRD analysis was designed to refine simultaneously both structural and microstructural parameters and the results are summarized in Table I (Fig. 2). In Figure 2, the calculated patterns are shown in the same field as a solid-line curve in blue. The difference between observed and calculated, is shown in the lower field in red. The observed results by Rietveld XRD pattern of the samples, matches well with the calculated one. No other new phases were observed. All refinements were performed using typical spinel phase crystal structure with a space group Fd3m. The refinement confirmed the spinel-type structure of the samples.[38–40] During the refinements, the goodness of fit is defined by $S = R_{wp}/R_e$, where R_{wp} and R_e, are, respectively, the R-weighted and the R-expected patterns. The obtained values of the lattice parameter and crystallite size from the Rietveld analysis are shown in Figure 3. Rietveld analysis show that all prepared samples had characteristic cubic spinel structure, but an increase of lattice parameters (lattice constant and unit-cell volume), due to Co incorporation into $ZnAl_2O_4$ lattice. The lattice parameter almost linearly increases by the addition of Co^{2+} content, thus obeying Vegard's rule. However, the ionic radii for tetrahedrally coordinated Zn^{2+} (0.60 Å) and Co^{2+} (0.58 Å) as well as octahedrally coordinated Al^{3+} (0.53 Å) and Co^{3+} (0.65 Å), one can expect the substitution Co^{2+} for A-sites resulting in decrease of lattice parameters. However, in our present case lattice expansion is observed,

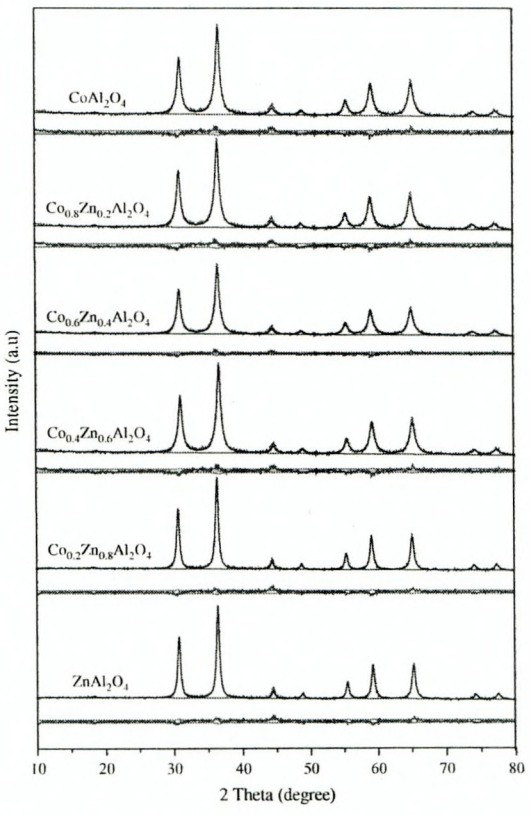

Figure 2. XRD pattern refinements using the Rietveld method of spinel $Co_xZn_{1-x}Al_2O_4$ ($x = 0.0$, 0.2, 0.4, 0.6, 0.8 and 1) nano-crystals.

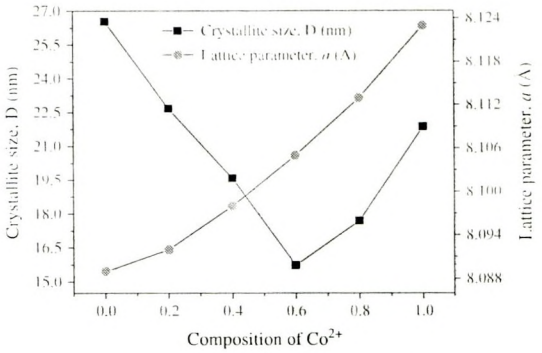

Figure 3. Lattice parameter and crystallite size (Scherer formula, Rietveld analysis) values of spinel $Co_xZn_{1-x}Al_2O_4$ ($x = 0.0$, 0.2, 0.4, 0.6, 0.8 and 1) nano-crystals.

which indicates that some amount of Co^{2+} should be in B-sites leads to inversion of spinel structure.[32, 36, 37] Such trend of $ZnAl_2O_4$ lattice expansion, due to Co doping has been reported already by Popovic et al.[40] Moreover, the general formula for Co-doped $ZnAl_2O_4$ can be written as $^{IV}(Co_{x-y}Zn_{1-x}Al_y)\ ^{VI}(Al_{2-y}Co_y)O_4$, where '$x$' represents the level of incorporated Co^{2+} cations in the $ZnAl_2O_4$ spinel structure, and 'y' is the inversion parameter of the spinel structure.[41] The differences in the results reported in the literature (lattice parameters and crystallites size) depend on the type of preparation methods, microwave treatment timing, and molar ratio of the starting precursors, nature and composition of dopant ions.

3.2. Fourier Transform Infrared (FT-IR) Analysis

FT-IR spectra of spinel $Co_xZn_{1-x}Al_2O_4$ ($x = 0.0$, 0.2, 0.4, 0.6, 0.8 and 1) nano-crystals are shown in Figures 4(a)–(f). Free water (H_2O) molecule has a strong and broad absorption band centered in the region 3120–3400 cm^{-1}. It can be seen that the bands at around 3430 cm^{-1} and at around 1631 cm^{-1} are present in all compositions, which can be assigned to the –OH stretching and H–O–H bending vibrations of adsorbed H_2O, respectively. The absorption band at 2342 cm^{-1} is due to the stretching vibration of CO_2 from atmosphere. The adsorbed H_2O can be distinguished from the –OH groups by the presence of H–O–H bending motion, which also produces a medium band in the region 1600–1650 cm^{-1}. However, the band at 1460 cm^{-1} is due to the stretching vibration of –N–H group. The bands at 553–912 cm^{-1} confirm the formation of normal spinel structure of $ZnAl_2O_4$. In all compositions of $ZnAl_2O_4$ samples, the metal-oxygen stretching frequencies are reported in the range 500–900 cm^{-1}, associated with the vibrations of M–O, Al–O and M–O–Al bonds (M = Zn, Co).[33] Generally, FT-IR spectra was measured in air atmosphere condition, which results in rapid adsorption of H_2O from the atmosphere, due to the very high surface area of the as-prepared spinel nano-crystals.[33]

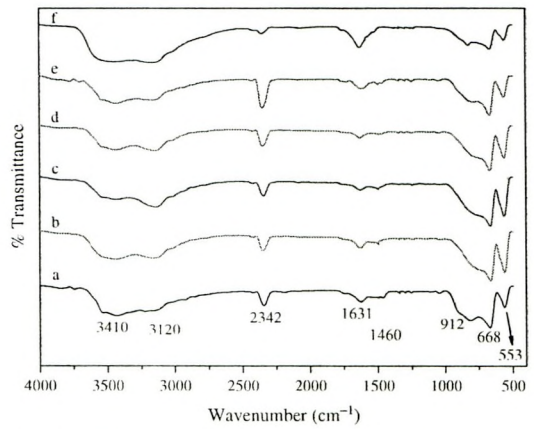

Figure 4. FT-IR spectra of (a) $ZnAl_2O_4$, (b) $Co_{0.2}Zn_{0.8}Al_2O_4$, (c) $Co_{0.4}Zn_{0.6}Al_2O_4$, (d) $Co_{0.6}Zn_{0.4}Al_2O_4$, (e) $Co_{0.8}Zn_{0.2}Al_2O_4$ and (f) $CoAl_2O_4$ nano-crystals.

3.3. Scanning Electron Microscopy (SEM) Studies

The high resolution scanning electron microscopy (HR-SEM) result shows that the morphologies of the nanocrystalline spinel $Co_xZn_{1-x}Al_2O_4$ ($x = 0.0$, 0.2, 0.4, 0.6, 0.8 and 1) powders. Figures 5(a)–(f) shows HR-SEM images of $ZnAl_2O_4$, $Co_{0.2}Zn_{0.8}Al_2O_4$, $Co_{0.4}Zn_{0.6}Al_2O_4$, $Co_{0.6}Zn_{0.4}Al_2O_4$, $Co_{0.8}Zn_{0.2}Al_2O_4$ and $CoAl_2O_4$, respectively. However, the surface morphologies of $Co_xZn_{1-x}Al_2O_4$ nano-crystals as seen from the HR-SEM consists of well developed particles with different shape and size of crystals with less uniform; varying size distribution with relatively well crystallized grain size smaller than 100 nm. Moreover, the particle with smaller porosity development is mainly due to the *Aloe vera* plant extract gelling solution for this combustion process. During the MCM process, the volatile gases such as N_2, CO_2, O_2, and H_2O as vapor phase escapes, and these are the main factors in creating such rudimentary pore structure in the spinel $Co_xZn_{1-x}Al_2O_4$ nano-crystals. However, the *Aloe vera* plant extract solution act as gelling as well as reducing agent in this method.

3.4. Transmission Electron Microscopy (TEM) Studies

The average crystallite size estimated from the XRD and Rietveld refinement XRD data agree with HR-TEM investigations. HR-TEM images of $Co_xZn_{1-x}Al_2O_4$ ($x = 0.2$ and 0.6) powders are provided in Figures 6(a)–(d). The small amount of agglomerations was observed in the HR-TEM micrographs. However, these nanoparticles are in the range of 16–27 nm in diameter; these values are in good agreement with the values obtained from XRD data. The selected area electron diffraction (SAED) patterns, presented in the Figures 6(e), (f), correspond to that of a spinel phase, confirm that the nano-crystals are composed of $ZnAl_2O_4$. The SAED pattern implies that the

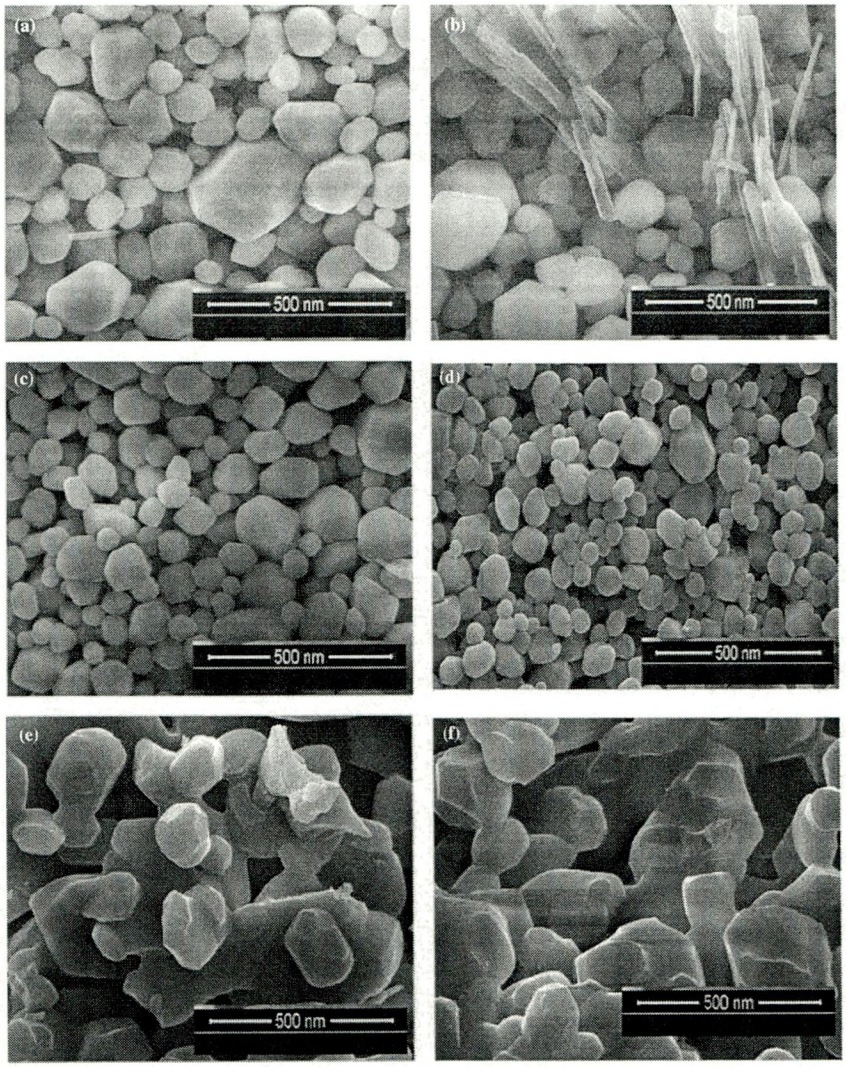

Figure 5. HR-SEM images of (a) $ZnAl_2O_4$, (b) $Co_{0.2}Zn_{0.8}Al_2O_4$, (c) $Co_{0.4}Zn_{0.6}Al_2O_4$, (d) $Co_{0.6}Zn_{0.4}Al_2O_4$, (e) $Co_{0.8}Zn_{0.2}Al_2O_4$ and (f) $CoAl_2O_4$ nano-crystals.

as-prepared spinel $ZnAl_2O_4$ nano-crystals are good crystalline materials and single crystalline in nature. From the HR-TEM image (Figs. 6(c) and (d)), it can be found that the $ZnAl_2O_4$ nano-crystals are cubic single crystalline and the distance between the two adjacent planes is approximately 0.264 nm ($Co_{0.2}Zn_{0.8}Al_2O_4$) and 0.273 nm ($Co_{0.6}Zn_{0.4}Al_2O_4$), respectively, which is in accordance with the (311) lattice fringes in the spinel nano-crystals, which is in agreement with the XRD results. In this present work, metal nitrates and Aloe vera plant extracted solution as the precursors are converted into single crystalline $ZnAl_2O_4$ nano-crystals, within 10 min, under the irradiation of microwaves.

3.5. Formation Mechanism of Spinel $Co_xZn_{1-x}Al_2O_4$ Nano-Crystals

The formation mechanism of spinel $Co_xZn_{1-x}Al_2O_4$ nano-crystals was proposed in Scheme 1. MCM route is one of the simplest techniques for preparing of numerous inorganic nanomaterials. In this present study, MCM approach was used successfully for synthesizing of $Co_xZn_{1-x}Al_2O_4$ nano-crystals; using metal nitrates and Aloe vera plant extract gelling solution as raw materials without any other catalyst and surfactants. In this combustion synthesis, Aloe vera plant extracted solution act as a complexing agent, which is homogeneously mixes with metal cations in atomic scale. It is believed that, during the combustion

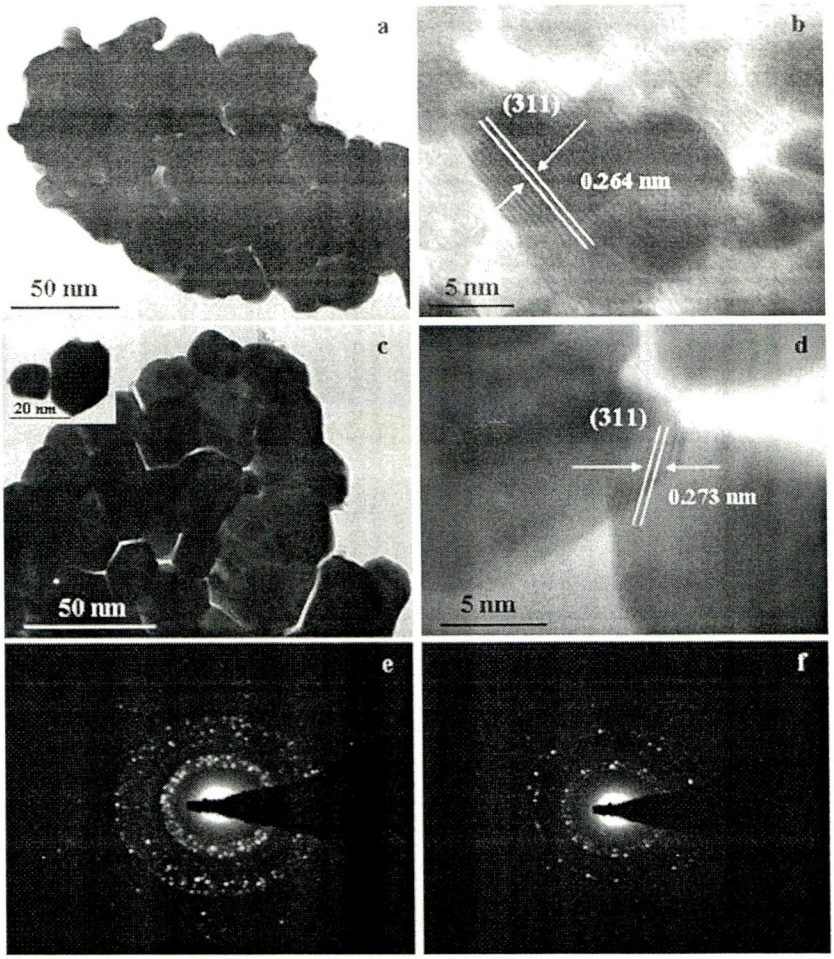

Figure 6. HR-TEM images and SAED patterns of $Co_{0.2}Zn_{0.8}Al_2O_4$ (a), (b), (e) and $Co_{0.6}Zn_{0.4}Al_2O_4$ (c), (d), (f) nano-crystals.

reaction, the microwave energy is used to nucleation growth of metallic Zn^{2+} and Al^{3+} cations mixture obtained with a very short time was subjected in the microwave irradiation. Consequently, when the resulting metal nuclei were oxidized quickly in a microwave irradiation treatment to formed products within few minutes of time with narrow size range was obtained.[18] Moreover, it is believed that Aloe vera plant extracted gelling solution here functions as a complexing and gelling agent in a solution and also acts as reducing agent. Interestingly, in this present study, when a mixed solution of Aloe vera plant extract and metal cations is subjected to microwave heating process, $Co_xZn_{1-x}Al_2O_4$ nano-crystals can be easily formed at low temperature with short reaction time. Thus, in the MCM process, nucleation and nuclei growth taking place, this facilitates obtaining nuclei with a narrow range of particle sizes. The results proved that the microwave irradiation method is a fast and easy synthesis method, due to that the microwave energy can directly interact with the material interior, which results in a well-developed nano-sized particles within few minutes of time and there is no need for further calcinations. However, the specific surface area of the sample prepared in MCM method is higher. This is due to the fact that the microwave irradiation is volumetric and homogeneous throughout the materials. Thus, it could be postulated that the microwave irradiation has an overall influence on the reaction rate, nanoparticle size and shape control. This method is simple and inexpensive one.

3.6. Energy Dispersive X-Ray (EDX) Studies

Energy dispersive X-ray (EDX) analysis of the as-prepared spinel $Co_xZn_{1-x}Al_2O_4$ nano-crystals is shown in Figure 7. Figures 7(a)–(d) shows the EDX spectra of $ZnAl_2O_4$, $Co_{0.4}Zn_{0.6}Al_2O_4$, $Co_{0.6}Zn_{0.4}Al_2O_4$ and $CoAl_2O_4$, respectively. EDX results showed that the peaks of Zn, Co, Al and O elements in $Co_xZn_{1-x}Al_2O_4$ nano-crystals and there

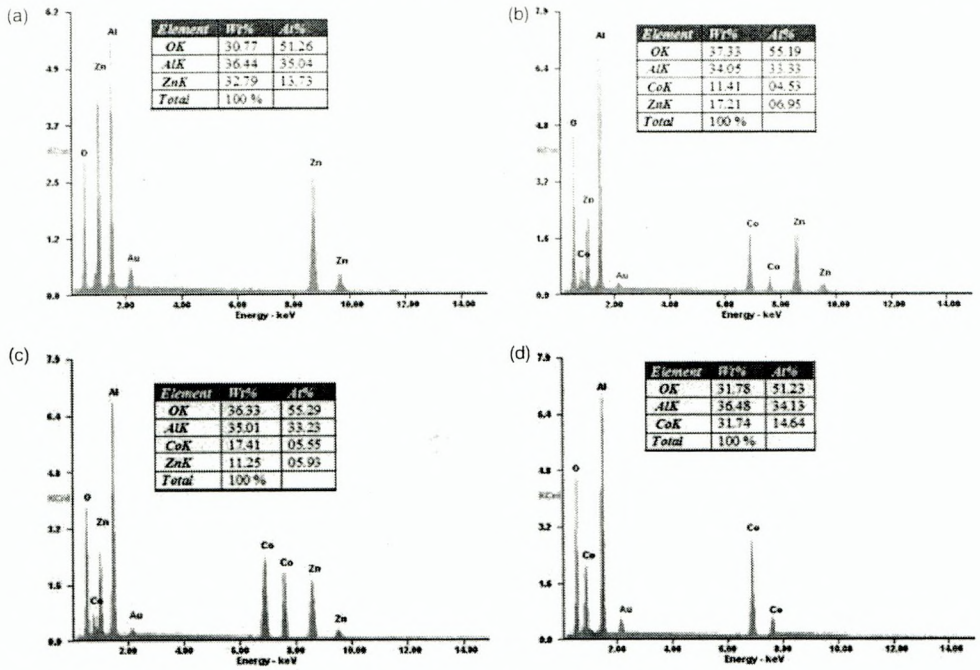

Figure 7. EDX spectra of (a) $ZnAl_2O_4$, (b) $Co_{0.4}Zn_{0.6}Al_2O_4$, (c) $Co_{0.6}Zn_{0.4}Al_2O_4$ and (d) $CoAl_2O_4$ nano-crystals.

is no other peak, which confirmed the as-prepared samples are pure. A small peak is appeared at 2.1 KeV for all the samples, which indicated the presence of gold (Au), which has been used as a sputter coating, while preparing the sample for HR-SEM analysis for the better visibility of the surface morphology.

3.7. N_2 Adsorption/Desorption Isotherms

In order to have an idea of the adsorbance competence of $Co_xZn_{1-x}Al_2O_4$ nano-crystals, BET surface area was determined using N_2 adsorption/desorption studies. However, BET studies revealed the specific relation between the concentration of the adsorbate and its adsorption degree onto the adsorbent surface. The N_2 adsorption/desorption isotherm values at 77 K of the spinel $Co_xZn_{1-x}Al_2O_4$ nano-crystals are given in Table II. It is well known that the surface area parameters of the samples varied according to the concentration of the Co dopant. However, the sample $Co_{0.6}Zn_{0.4}Al_2O_4$ spinel has highest surface area of 63.54 m^2/g than other samples. In MCM process, an efficient and a homogeneous heating would result in a rapid and uniformity nucleation followed by the growth of spinel $Co_xZn_{1-x}Al_2O_4$ nano-crystals. In general, due to the microwave irradiation, the speed of nucleation and growth, this smaller will be the size of the $Co_xZn_{1-x}Al_2O_4$ nano-crystals. However, MCM reaction is completed within few minutes in a domestic microwave oven with the temperature ranges 150–400 °C. Within the limited time with low temperature, nucleation and growth has to be finished, due to the homogeneous distribution of microwave energy to the material interior. Hence, the high surface area of the nano-crystals with smaller and narrow distribution.

Table II. BET surface area, average pore diameter and pore volume of spinel $Co_xZn_{1-x}Al_2O_4$ ($x = 0.0$, 0.2, 0.4, 0.6, 0.8 and 1) nano-crystals.

Samples	BET surface area (m^2/g)	Average pore radius (Å)	Total pore volume (cm^3/g)
$ZnAl_2O_4$	37.22	82.54	0.185
$Co_{0.2}Zn_{0.8}Al_2O_4$	40.43	84.67	0.174
$Co_{0.4}Zn_{0.6}Al_2O_4$	48.35	85.97	0.161
$Co_{0.6}Zn_{0.4}Al_2O_4$	63.54	92.17	0.142
$Co_{0.8}Zn_{0.2}Al_2O_4$	58.79	87.85	0.153
$CoAl_2O_4$	55.95	85.64	0.159

3.8. Diffuse Reflectance Spectroscopy (DRS)

The fundamental process of UV-Visible absorption or reflectance or transmittance of light by nano-sized semiconducting metal oxides is significant to their electronic structures. Hence, the UV-Visible diffuse reflectance spectroscopy (DRS) studies play a vital role in estimating the band gap energy. The optical band gap energy was calculated using Tauc relation.[15] The Kubelka-Munk function is generally applied to convert the diffuse reflectance into equivalent absorption coefficient and mostly used for analyzing the powder samples.[42] The Kubelka-Munk function

$F(R)$ was used to calculate the band gap energy of the nanocrystalline $Co_xZn_{1-x}Al_2O_4$ samples. Thus the vertical axis is converted into quantity $F(R)$ which is equal to the absorption co-efficient. Thus the 'α' in the Tauc equation is substituted with $F(R)$ and hence the relation becomes,

$$(F(R)) = \alpha = \frac{(1-R)^2}{2R} \tag{5}$$

where, $F(R)$ is Kubelka-Munk function, 'α' the absorption coefficient, 'R' the reflectance. Thus the Tauc relation becomes,

$$F(R)h\upsilon = A(h\upsilon - E_g)^n \tag{6}$$

where $n = 1/2$ and 2 for direct and indirect transitions, respectively, thus giving direct and indirect band gaps. The plots of $(F(R)h\upsilon)^2$ versus $h\upsilon$ for all compositions are shown in Figure 8. Extrapolation of linear regions of these plots to $(F(R)h\upsilon)^2 = 0$ gives the direct band gap values.

The optical band gap energy values for all composition of $Co_xZn_{1-x}Al_2O_4$ as shown in Table I (Fig. 9). The direct band gap value of the pure $ZnAl_2O_4$ was observed to be 4.12 eV, which is higher than the reported value of bulk spinel $ZnAl_2O_4$ (i.e., 3.8 eV), suggesting a blue shift which may be due to quantum confinement phenomena. The observed higher band gap energy is due to smaller size of $ZnAl_2O_4$ particles.[43] Conversely, the band gap energy decreases from 3.92 to 3.67 eV with increase in Co^{2+} content ($x = 0.2$ to 1) in $ZnAl_2O_4$ matrices. However, this kind of band gap narrowing trend have been observed by Ming et al.[44] and Ahmed et al.[45] for doped SnO_2 nano particles. This detail can be associated to the difference in the electronic structure of the Co^{2+} dopant. The decrease in band gap may also be due to the sp-d exchange interaction between the localized d-electrons of Co^{2+} ions and band electrons of $ZnAl_2O_4$. Thus, the contraction band gap with Co doping could be due to the formation of sub-bands in between the energy band gap and merging of their sub-bands with the conduction band to form a continuous band.[45]

3.9. Photoluminescence (PL) Studies

The photoluminescence (PL) spectra were recorded to investigate the recombination phenomena in the metal oxide semiconductors. Moreover, PL spectrum gives the information about the band gap with the relative active position of sub band gap defect states of the metal oxide semiconductors.[46] Generally, $ZnAl_2O_4$ is employed as the ceramic material, and doped with transition metals (e.g., Cu and Co) as the activator and co-activator. Cheng et al.[47] reported the room temperature PL properties of $ZnAl_2O_4$ samples doped with Eu^{3+}. However, in this present study, we have reported the PL properties of $ZnAl_2O_4$ spinel doped with Co^{2+}. Figure 10 demonstrates the room temperature PL spectra recorded at $\lambda_{ex} = 220$ nm of $ZnAl_2O_4$ samples prepared with various doping concentration of Co^{2+} content and observed emission bands in UV as well as in the visible regions. A small band is observed at 301 nm is ascribed to the near band-edge (NBE) emission of wide band gap of $ZnAl_2O_4$ due to the recombination of free excitons through an exciton–exciton process.

The estimated band gap (4.12 eV) from the NBE emission is in agreement with the band gap estimated from Kubelka-Munk plot derived from the DRS spectra. Chen et al.[11] have reported the PL results of $ZnAl_2O_4$ at $\lambda_{ex} = 220$ nm without doping any metals, and they observed broad emission bands centered at 323 nm, which are in agreement with the band gap of bulk $ZnAl_2O_4$ (i.e., 3.8 eV). In the present study, spinel $Co_xZn_{1-x}Al_2O_4$ ($x = 0.0$, 0.2, 0.4, 0.6, 0.8 and 1) samples shows a peak corresponding to violet emission centered at 443 nm, due to the radiating defects related to the interface traps existing at the grain boundaries. Also, blue emissions (459 and 485 nm) appeared, which represent a deep level visible emissions associated with localized levels in the band gap.[48] A green emission centered at 543 nm, may be ascribed to the oxygen vacancies. It is found from the PL spectra that the emission characteristics are governed by the defect controlled processes.

However, it is observed that the doping of Co^{2+} in $ZnAl_2O_4$ structure decreases the luminescence intensity with an increase in x values. Although, the defect controlled processes in all compositions the PL intensity decreases, due to the decrease in distance between the dopant (activator) and the array. Thus, the results are suggestive that the various emissions in the $Co_xZn_{1-x}Al_2O_4$ spinel arises, due to the defect centers that act as trap levels, which leads to the appearance of new electronic energy levels between the valence and the conduction band.

3.10. Magnetic Measurements

The magnetization behavior of $Co_xZn_{1-x}Al_2O_4$ ($x = 0.0$, 0.2, 0.4, 0.6, 0.8 and 1) nano-crystals were investigated by sweeping the external magnetic field between ±15 kOe at 300 K using room temperature vibrating sample magnetometer (VSM). Magnetizations (M) versus magnetic field (H) behavior plots are shown in Figure 11 and the values are summarized in Table III. These curves are typical for a soft magnetic material and indicate hysteresis dia, superpara and ferromagnetism in the field ranges of ±15 kOe. The inset in Figure 11 shows the magnetic behavior of $CoAl_2O_4$. The observed saturation magnetization (M_s), remanent magnetization (M_r) and coercivity (H_c) values are reported in Table III. A small hysteresis was observed for $ZnAl_2O_4$ sample shows horizontal line with small hysteresis curve indicating a diamagnetic behavior. However, the doping of magnetic nature of Co^{2+} ions in Zn^{2+} sites leads $ZnAl_2O_4$ to possess magnetic property. All the Co^{2+} doped $ZnAl_2O_4$ ($x = 0.2$, 0.4, 0.6, 0.8 and 1) nano-crystals display 'hysteresis' type curve. This is a typical behavior of superparamagnetism for Co^{2+} doped $ZnAl_2O_4$ ($x = 0.2$, 0.4, 0.6 and 0.8) nano-crystals,

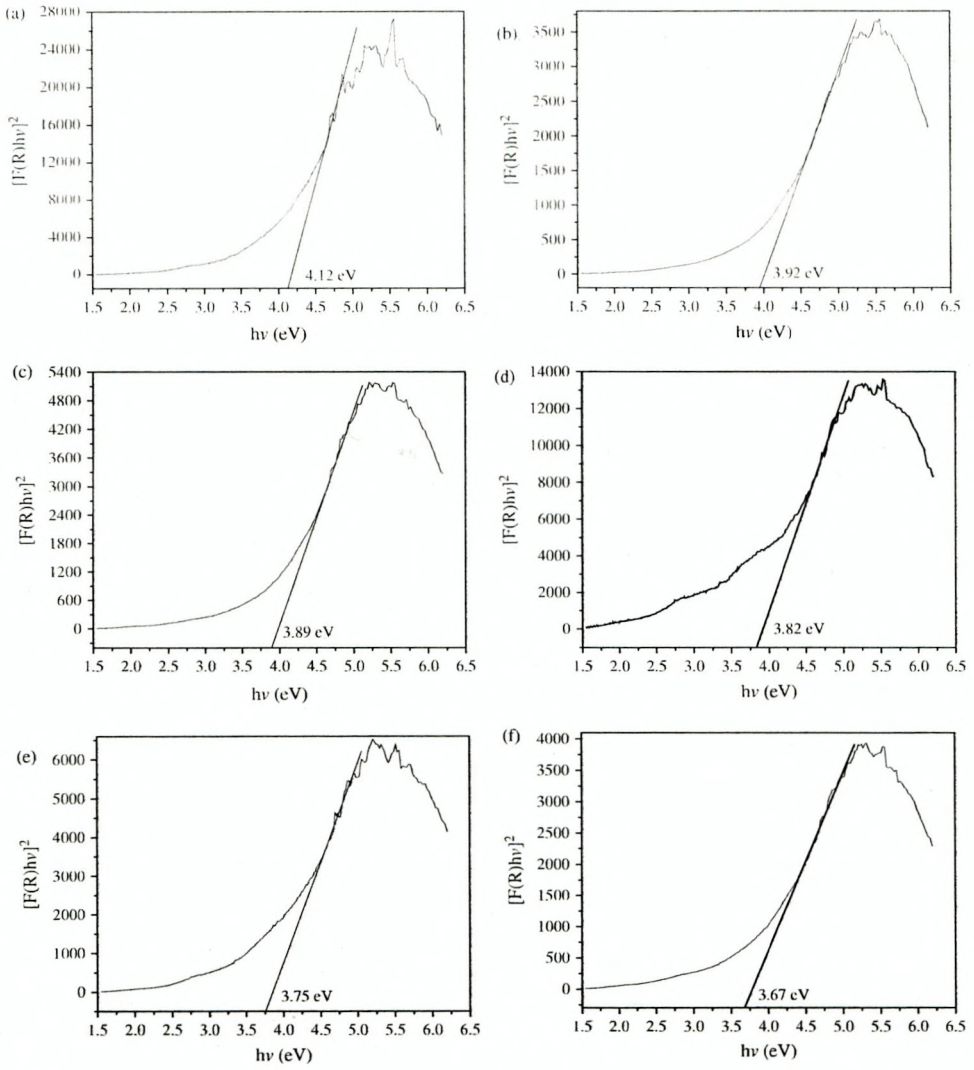

Figure 8. UV-Vis DRS spectra of (a) $ZnAl_2O_4$, (b) $Co_{0.2}Zn_{0.8}Al_2O_4$, (c) $Co_{0.4}Zn_{0.6}Al_2O_4$, (d) $Co_{0.6}Zn_{0.4}Al_2O_4$, (e) $Co_{0.8}Zn_{0.2}Al_2O_4$ and (f) $CoAl_2O_4$ nano-crystals.

whereas, pure $CoAl_2O_4$ nano-crystals show the ferromagnetic behavior, where magnetization increased with the applied field and does not saturate even at ±15 kOe. Thus, in the present study, introducing Co^{2+} as a dopant in the $ZnAl_2O_4$ matrix, leads to the conversion of diamagnetism ($ZnAl_2O_4$) into superparamagnetic (Co^{2+} doped $ZnAl_2O_4$: $x = 0.2$, 0.4, 0.6 and 0.8) and then ferromagnetic ($CoAl_2O_4$) material with increasing the specific saturation magnetization (M_s). The observed magnetic property might be due to the combination of the particle size and cobalt ion doping. When the spinel $Co_xZn_{1-x}Al_2O_4$ nano-crystals were formed by the heating of microwaves, more oxygen defects or zinc vacancies were formed on the surface of the particles and these defects could cause and results that the Al^{3+} occupied A-sites more easily, despite Co^{2+} ions can occupy B-sites. The antisites of Al^{3+} ions in sites of Co^{2+} cause the charge unbalanced, in order to balance the charge in the nano-crystals, the electrons of the nearest neighboring O_2^- close to the Al^{3+}, which cause the spin polarization and result in the ferromagnetism.

However, it is observed that H_c and M_s values of the spinel $Co_xZn_{1-x}Al_2O_4$ nano-crystals gradually increased with the increase of Co^{2+} content ($x = 0.2$ to 1.0) this can be attributed to the non-magnetic nature of Zn^{2+} substituted by magnetic nature of Co^{2+}. The obtained result show that the value of M_s is lower (0.057 emu/g) for pure

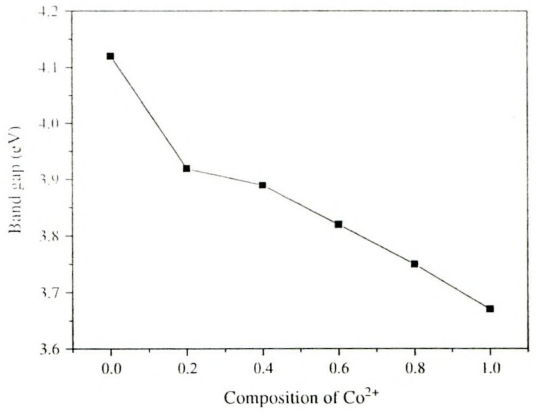

Figure 9. Band gap values of $Co_xZn_{1-x}Al_2O_4$ ($x = 0.0$, 0.2, 0.4, 0.6, 0.8 and 1) nano-crystals.

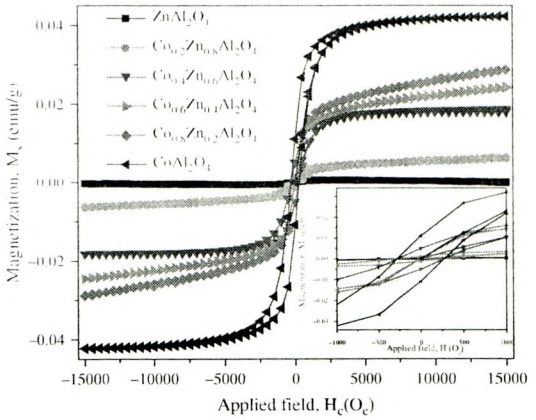

Figure 11. Magnetic hysteresis (M–H) loops of $Co_xZn_{1-x}Al_2O_4$ ($x = 0.0$, 0.2, 0.4, 0.6, 0.8 and 1) nano-crystals.

$ZnAl_2O_4$, and it is increased from 6.571 to 42.53 emu/g with increase the concentration of Co^{2+} ($x = 0.2$ to 1.0), which can be attributed to the non-magnetic nature of Zn^{2+} ions (0 μB) substituted by the higher magnetic moments of Co^{2+} (3 μB) ions at the octahedral (B-) sites. Norton et al.[49] and Park et al.[50] also reported that magnetic nature of Co^{2+} doped ZnO have superparamagnetic properties assigned to Co nano-cluster. It is well known that M_s value of the magnetic material is dependent on the size, morphology and structure of the samples.[51–55]

3.11. Catalytic Test

It is well known that the catalytic activity of nano-materials depends strongly on particle size, morphology and microstructure. The preparation and characterization of nano-crystals with well-controlled size, shape and chemical homogeneity are important for catalytic purposes.[56–58] In the present study, the catalytic study showed that the nature and concentration of the dopant ions had a strong influence on both the conversion and product selectivity. The catalytic results were summarized in Table IV. In general, the resultants the spinel aluminates display clear difference in the selective oxidation of benzyl alcohol. In order to find efficient results for the catalytic oxidation of benzyl alcohol, the reaction environments were altered by studying the effect of surface area, effect of particle size, effect of sample composition ($x = 0.0$ to 1.0), effect of catalyst amount (0.1–0.8 g), effect of reaction time (1–5 h), effect of oxidant and solvents.

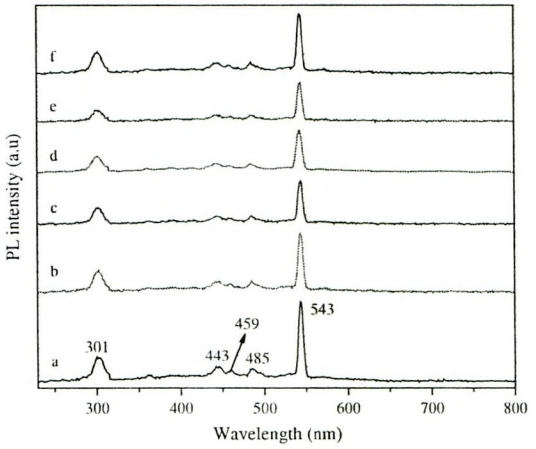

Figure 10. PL spectra of (a) $ZnAl_2O_4$, (b) $Co_{0.2}Zn_{0.8}Al_2O_4$, (c) $Co_{0.4}Zn_{0.6}Al_2O_4$, (d) $Co_{0.6}Zn_{0.4}Al_2O_4$, (e) $Co_{0.8}Zn_{0.2}Al_2O_4$ and (f) $CoAl_2O_4$ nano-crystals.

3.11.1. Effect of Surface Area

Generally, the catalyst with a high specific surface area has a favorable effect on the catalytic activity. In this present work, the surface area of $Co_xZn_{1-x}Al_2O_4$ ($x = 0.0$, 0.2, 0.4, 0.6, 0.8 and 1) nano-catalysts gradually increased with increase of Co^{2+} content until $x = 0.6$, and rapidly decreased for x larger than 0.6, i.e., $x = 0.8$ and 0.1 (Table II), this can be attributed to the magnetic character, and the anisotropic nature of Co^{2+} ions replaced the non-magnetic nature of Zn^{2+} ions. The sample

Table III. Magnetic properties (magnetization, remanant and coercivity) of spinel $Co_xZn_{1-x}Al_2O_4$ ($x = 0.0$, 0.2, 0.4, 0.6, 0.8 and 1) nano-crystals.

Samples	Coercivity, H_c (Oe)	Retentivity, M_r ($\times 10^{-3}$) (emu/g)	Magnetization, M_s ($\times 10^{-3}$) (emu/g)
$ZnAl_2O_4$	24.94	0.132	0.057
$Co_{0.2}Zn_{0.8}Al_2O_4$	63.78	1.175	6.571
$Co_{0.4}Zn_{0.6}Al_2O_4$	92.61	1.463	18.35
$Co_{0.6}Zn_{0.4}Al_2O_4$	164.6	1.836	24.46
$Co_{0.8}Zn_{0.2}Al_2O_4$	214.9	5.289	28.92
$CoAl_2O_4$	283.7	11.16	42.53

Table IV. The conversion and selectivity percentage for the oxidation of benzyl alcohol to benzaldehyde (reaction conditions: Catalyst ($Co_xZn_{1-x}Al_2O_4$, where $x = 0.0$, 0.2, 0.4, 0.6, 0.8 and 1), 0.5 g; Benzyl alcohol, 5 mmol; Acetonitrile, 5 mmol; H_2O_2, 5 mmol; Temperature, 80 °C, time, 5 h).

Samples	Conversion (%)	Selectivity (%)
$ZnAl_2O_4$	86.31	92.85
$Co_{0.2}Zn_{0.8}Al_2O_4$	89.64	94.32
$Co_{0.4}Zn_{0.6}Al_2O_4$	92.53	95.56
$Co_{0.6}Zn_{0.4}Al_2O_4$	93.25	99.56
$Co_{0.8}Zn_{0.2}Al_2O_4$	81.58	91.79
$CoAl_2O_4$	80.56	90.24

$Co_{0.6}Zn_{0.4}Al_2O_4$ had higher surface area (63.54 m^2/g) than other samples, due to the smaller particle size of $Co_{0.6}Zn_{0.4}Al_2O_4$ nano-catalyst. Furthermore, the sample $Co_{0.6}Zn_{0.4}Al_2O_4$ showed better catalytic activity than other samples (Fig. 12). However, the high surface area of $Co_{0.6}Zn_{0.4}Al_2O_4$ nano-particle was useful to catalytic activity via enhancing the adsorption of benzyl alcohol, which is the determining step in the catalytic reaction.[59] It was found that the conversion of benzyl alcohol into benzaldehyde for the sample $Co_{0.6}Zn_{0.4}Al_2O_4$ was 93.25% with 99.56% selectivity, whereas the undoped $ZnAl_2O_4$ sample, the conversion was only 86.31% with 92.85% selectivity. However, the $Co_{0.6}Zn_{0.4}Al_2O_4$ catalyst with high surface area displays the best performance in the selective oxidation of benzyl alcohol to benzaldehyde.

3.11.2. Effect of Particle Size

The particle size of spinel $Co_xZn_{1-x}Al_2O_4$ ($x = 0.0$, 0.2, 0.4, 0.6, 0.8 and 1) nano-catalysts play an important role in the catalytic activity. Besides, as the particle size decreases, the number of surface active sites increases in the catalysts. Thus, it is expected that the sample $Co_{0.6}Zn_{0.4}Al_2O_4$ nano-particles with very smaller particle size distribution would be a potentially efficient catalyst (Fig. 12), due to the larger surface area coverage and better adsorption behavior, which in turn leads to the efficient catalysis. However, the sample $Co_{0.6}Zn_{0.4}Al_2O_4$ nano-catalysts had smaller particle size distribution, as indicated by the XRD, Rietveld and HR-SEM data, which showed considerably higher catalytic activity for the oxidation of benzyl alcohol than other samples. In addition, when the size of particles decreases, the amount of dispersion of particles per volume in the solution will increase, this results the enhancement of catalytic activity. Therefore, the catalytic activity of $Co_{0.6}Zn_{0.4}Al_2O_4$ nano-particle is higher than the other samples. Although, the differences in the activities of spinel $Co_xZn_{1-x}Al_2O_4$ nano-catalysts in terms of conversion and product yield are remarkable and the reaction time was shortened in case of catalysts with higher surface area. Thus, it is obvious that the activity of spinel $Co_xZn_{1-x}Al_2O_4$ nano-catalysts depend on the preparation methods. The sample $Co_{0.6}Zn_{0.4}Al_2O_4$ had higher surface area (63.54 m^2/g) than other samples, due to smaller particle size. In addition, when the size of particles decreases, the amount of the dispersion of particles per volume in the solution will increase, and the sample $Co_{0.6}Zn_{0.4}Al_2O_4$ provide more contact area for the reactants and catalysts, which is mainly due to their high surface-to-volume ratio with higher surface area when compared to other samples.[59]

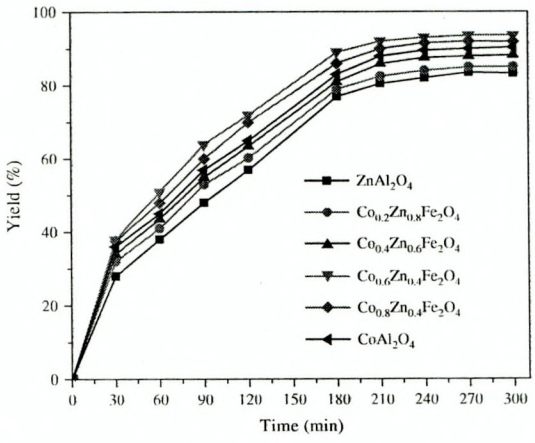

Figure 12. Catalytic activities (reaction conditions: Catalyst ($Co_xZn_{1-x}Al_2O_4$, where $x = 0.0$, 0.2, 0.4, 0.6, 0.8 and 1), 0.5 g; Benzyl alcohol, 5 mmol; Acetonitrile, 5 mmol; H_2O_2, 5 mmol; temperature, 80 °C, time, 5 h).

3.11.3. Effect of Sample Composition

The sample composition of spinel $Co_xZn_{1-x}Al_2O_4$ ($x = 0.0$, 0.2, 0.4, 0.6, 0.8 and 1) nano-catalysts play an important role in the catalytic activity. In order to study the effect of sample composition on the activity of the catalyst, various doping concentration of Co^{2+} ions were substituted in $ZnAl_2O_4$ and used as catalysts and the results are given in Figure 12 (Table IV). The reaction was also studied with the pure $ZnAl_2O_4$, under similar conditions. Pure $ZnAl_2O_4$ shows poor activity in terms of the yield for the oxidation of benzyl alcohol. It was observed that the catalytic activity varied with the amount of substituent of Co^{2+} ions. The $Co_{0.6}Zn_{0.4}Al_2O_4$ sample showed maximum yield of the benzaldehyde among all other compositions. Generally, Co^{2+} plays a crucial role in the H_2O_2 decompositions, which was confirmed in the previous literatures[60, 61] where the finally produced O_2 would greatly benefit for the oxidation of benzyl alcohol. Another possible reason was due to the uniform structure and smaller size with high surface area of $Co_{0.6}Zn_{0.4}Al_2O_4$ nano-crystals. Moreover, the sample $Co_{0.6}Zn_{0.4}Al_2O_4$ provide more contact area for the reactants and catalyst, which is mainly due to their high surface-to-volume ratio with higher surface area when compared to the pure $ZnAl_2O_4$. Therefore, the greater catalytic activity of sample $Co_{0.6}Zn_{0.4}Al_2O_4$, when compared

to the activity of other samples, can be attributed to the better coordination of the carbonyl group to nano-sized spinels, due to the participation of more surface sites in the reaction. However, pure $ZnAl_2O_4$ and pure $CoAl_2O_4$, relatively poor performance was detected, which were possible due to their bigger particle size with lower surface area.[62] Usually, the catalytic oxidation of benzyl alcohol to produces a mixture of benzaldehyde, benzoic acid and benzyl benzoate. However, benzoic acid and benzyl benzoate were not obtained in our present study. Therefore, the catalyst was found to be highly selective.

3.11.4. Effect of Reaction Time

In order to prove the catalytic activity of the as-prepared spinel nano-catalysts, the oxidation of benzyl alcohol was carried out using H_2O_2 as the oxidant along with 0.5 g catalyst using acetonitrile as the solvent. Reaction time is very important to measure the activity of catalyst. Product analysis was carried out at different time intervals of 30, 60, 90, 120, 180, 210, 240, 270 and 300 minutes. Figure 12 shows the effect of reaction time on the conversion of benzyl alcohol into benzaldehyde using $Co_xZn_{1-x}Al_2O_4$ ($x = 0.0$, 0.2, 0.4, 0.6, 0.8 and 1) nano-catalysts. The result indicates that the conversion increased almost linearly with reaction time up to 180 min and then increased slowly from 180 to 240 min. The slower rate period from 30–180 min may be due to the competitive adsorption of the product (benzaldehyde) molecules on the active sites of the catalyst which may hinder the incoming benzyl alcohol molecules to participate in further reaction.[63] It is observed that at 240 min of catalytic test, saturation is reached which may be due to the saturation of the adsorption of molecules in the pores of the sample. The conversion was found to be nearly same for the 240 and 300 min experiments, indicating the constant conversion after 240 min. No appreciable change in the oxidation of benzyl alcohol to benzaldehyde was observed when running the reaction for 300 min. Similar results were reported earlier by Ali et al.[64] The only product of benzaldehyde was obtained from these nano-catalysts. But the catalyst surface gets regenerated by the action of the H_2O_2 (oxidant) with the catalyst, which leads to desorption of the product molecules, thereby favoring further oxidation.

3.11.5. Effect of Catalyst Amount

Figure 13 shows the effect of the amount of $Co_{0.6}Zn_{0.4}Al_2O_4$ catalyst on the conversion and selectivity towards the oxidation of benzyl alcohol into benzaldehyde (Table V). With an increase in the amount of catalyst from 0.1 to 0.5 g, the conversion of benzaldehyde is increased from 65.32% to 93.25%, the conversion and yield remain nearly the same, which suggests that large amount of catalyst, is not needed to improve the reaction product. The conversion of benzyl alcohol into benzaldehyde was found to increase considerably upon increasing

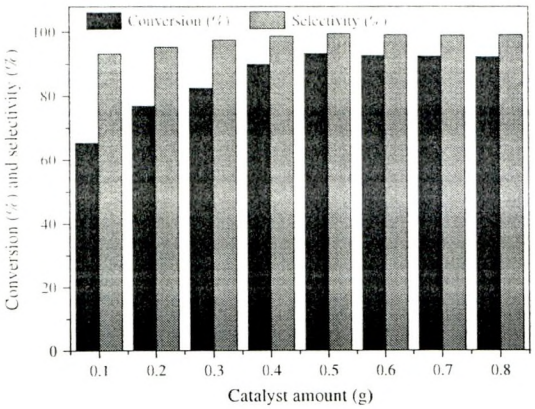

Figure 13. The amount of spinel $Co_{0.6}Zn_{0.4}Al_2O_4$ catalyst on the conversion and selectivity towards the oxidation of benzyl alcohol to benzaldehyde (reaction conditions: Catalyst ($Co_{0.6}Zn_{0.4}Al_2O_4$: 0.1 to 0.8 g); Benzyl alcohol, 5 mmol; Acetonitrile, 5 mmol; H_2O_2, 5 mmol; Temperature, 80 °C, time, 5 h).

the catalyst amount upto 0.5 g, while it remained almost unchanged when increasing the amount of catalyst 0.6 to 0.8 g. However, it was found that with the increase of catalyst amount the conversion and yield increased upto 0.5 g. This may apparently due to the availability of more active sites of the catalyst. Increasing the catalyst amount, improved the conversion efficiency upto 93.25% (0.5 g) within 5 h of time, which indicates that the increase in the catalyst, increase the catalytic active sites and thus accelerated the conversion of the substrates. Therefore, the optimized catalyst amount for the reaction is 0.5 g. Therefore, the present study indicate that an appropriate conversion and selectivity was obtained even with the small amount of catalyst 0.5 g. Oxidation over $Co_{0.6}Zn_{0.4}Al_2O_4$ nano-catalyst using eco-friendly oxidants, such as, hydrogen peroxide is preferred recently for environmental and economic benefits. Thus, an effective route is achieved for the conversion of benzyl alcohol into benzaldehyde using $Co_{0.6}Zn_{0.4}Al_2O_4$ nano-catalyst with better selectivity.

Table V. The conversion and selectivity percentage for the oxidation of benzyl alcohol to benzaldehyde (reaction conditions: Catalyst (0.1, 0.2, 0.3, 0.4, 0.5, 0.6, 0.7 and 0.8 g); Benzyl alcohol, 5 mmol: Acetonitrile, 5 mmol; H_2O_2, 5 mmol; Temperature, 80 °C, time, 5 h).

Catalyst amount (g)	Conversion (%)	Selectivity (%)
0.1	65.32	93.21
0.2	76.81	95.25
0.3	82.54	97.53
0.4	89.93	98.74
0.5	93.25	99.56
0.6	92.68	99.13
0.7	92.49	99.01
0.8	92.21	99.11

3.11.6. Effect of the Oxidant and the Solvent

In the absence of oxidant, the formation of benzaldehyde was not observed. This evidently ruled out the possibility of the reaction occurring, due to the participation of lattice oxygen alone. Hence the reaction was subsequently carried out in presence of H_2O_2 oxidant. H_2O_2 oxidant showed significant yields in acetonitrile medium, due to the formation of peroxycarboximidic acid intermediate which is a good oxygen transfer agent. In the absence of solvent, very low amount of benzaldehyde formation was observed (2%). Consequently, the reaction was carried out using acetonitrile solvent. The highest yield of benzaldehyde (93.25%) was observed for $Co_{0.6}Zn_{0.4}Al_2O_4$ nano-catalyst using H_2O_2 as the oxidant in acetonitrile medium. Acetonitrile can activate peroxide by forming a perhydroxyl anion (OOH^-) that nucleophilically attacks the nitrile to generate a peroxycarboximidic acid intermediate, which is a good oxygen transfer agent. Both organic substrate as well as the oxidant H_2O_2 dissolves in acetonitrile forming a uniform solution.[65]

3.11.7. Proposed Catalytic Reaction Mechanism

In this present study, spinel $Co_xZn_{1-x}Al_2O_4$ ($x = 0.0$, 0.2, 0.4, 0.6, 0.8 and 1) nano-catalysts were prepared by a simple MCM technique, has proved to be powerful for the selective and environmentally caring benzyl alcohol oxidation. The proposed mechanism for spinel $Co_xZn_{1-x}Al_2O_4$ catalyzed reaction of acetonitrile medium is shown in Scheme 2. Initially, solvent acetonitrile can activate H_2O_2 by forming a perhydroxyl anion (OOH^-), which nucleophilically attacks the nitrile to generate an intermediate peroxycarboximidic acid. It well known that the formed intermediate is a good oxygen transfer agent. The organic substrate (benzyl alcohol) and the oxidant H_2O_2 dissolves in acetonitrile, which activate H_2O_2 to OOH^- anion and forming Zn–OOH species.[66] This account revealed that the phenyl ring and the OH group of benzyl alcohol interact with Zn^{2+} ion of $ZnAl_2O_4$ and the inner active sites remains intact. The interaction of phenyl ring and OH group with the outer metal ions of $ZnAl_2O_4$ is also evident by the adsorption of phenyl ring on $ZnAl_2O_4$. However, the catalyst surface gets regenerated by the action of the oxidant with catalyst, which leads to desorption of the product molecules, thereby favoring further oxidation. Hence, this process is of great interest for the selective oxidation of benzyl alcohol into benzaldehyde. It is noted that not only the conversion of benzyl alcohol, but also the benzaldehyde selectivity was higher for the sample $Co_{0.6}Zn_{0.4}Al_2O_4$. In addition, H_2O_2 has been proved to be very efficient and environmentally friendly oxidant, since the product is only aldehyde.[64]

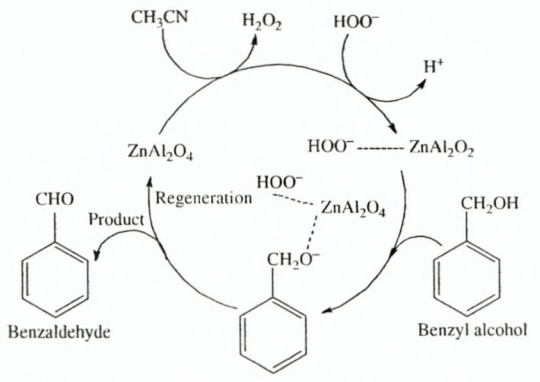

Scheme 2. Schematic diagram of catalytic oxidation of benzyl alcohol into benzaldehyde by spinel $Co_xZn_{1-x}Al_2O_4$ ($x = 0.0$, 0.2, 0.4, 0.6, 0.8 and 1) nano-catalysts.

3.12. Reusability Studies

The catalytic oxidation of benzyl alcohol into benzaldehyde was employed as a model reaction to investigate the reusability of spinel $Co_{0.6}Zn_{0.4}Al_2O_4$ nano-catalyst. The recycling of nano-catalyst is very important for industrial and technological applications. The reusability of nano-catalyst for the liquid phase oxidation of benzyl alcohol into benzaldehyde was evaluated and the results are shown in Figure 14. The percentage yield versus number of cycles for the reusability of $Co_{0.6}Zn_{0.4}Al_2O_4$ nano-catalyst is shown in Figure 14. For this purpose, the sample was filtered off from each run and washed several times with ethanol and dried at 120 °C in an air oven for 3 h and was checked for five consecutive runs under the same conditions. During the five runs investigated, the conversion of benzyl alcohol was in a range from 93.25 to 92.83% for the sample $Co_{0.6}Zn_{0.4}Al_2O_4$, indicating that the catalyst displays good reproducibility and stability. Interestingly the formation of benzoic acid was not detected. Since

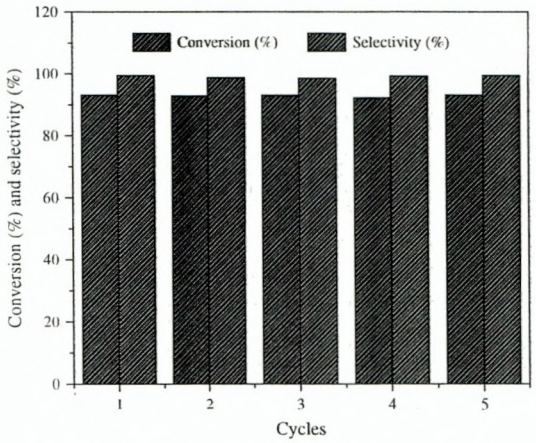

Figure 14. The reusability of the catalyst for the oxidation of benzyl alcohol to benzaldehyde.

the spinel $Co_{0.6}Zn_{0.4}Al_2O_4$ nano-catalyst is able to oxidize benzyl alcohol into benzaldehyde with high activity, highly recyclable, remarkably stable and environmental friendly, they are promising candidates for the industrial applications.

4. CONCLUSIONS

Spinel $Co_xZn_{1-x}Al_2O_4$ ($x = 0.0$, 0.2, 0.4, 0.6, 0.8 and 1) nano-crystals were successfully prepared by a simple MCM route using metal nitrates and *Aloe vera* plant extract solution as raw materials. The effect of Co^{2+} doping on the structural, morphological, optical and magnetic properties was investigated and also the catalytic activity for the selective oxidation of benzyl alcohol was investigated. Powder XRD pattern suggested the formation of pure gahnite in all the Co^{2+} doped $ZnAl_2O_4$ matrices. The precious crystallite size estimated from Rietveld refinement XRD method is good agreement with the results obtained through the Scherrer's method. Also, the XRD, EDX and SAED results indicate that the as-synthesized $Co_xZn_{1-x}Al_2O_4$ nano-crystals have spinel structure without the presence of any other phase impurities. The appearance of two bands between 500 and 900 cm^{-1} in FT-IR spectra revealed the formation of spinel structure. HR-SEM and HR-TEM images depicted the formation of well developed particle-like crystal morphology with nano-sized grains. UV-Visible DRS results showed the band gap energy of pure $ZnAl_2O_4$ is 4.12 eV and it is decreased from 3.89 eV to 3.67 eV with increasing the Co-dopant ($x = 0.2$–1.0), indicating quantum confinement phenomena, also, due to the formation of sub band gaps. PL spectra of pure and Co^{2+}-doped $ZnAl_2O_4$ nano-crystals suggested defect controlled processes. VSM study revealed that the doping of Co^{2+} in $ZnAl_2O_4$ can bring in diamagnetism to superparamagnetic and then ferromagnetic behavior. It was found that $Co_{0.6}Zn_{0.4}Al_2O_4$ is highly active towards the selective oxidation of benzyl alcohol into benzaldehyde at low temperature with high yields (99.56%), because of the higher surface area and presence of more number of active sites, due to the influence of addition of *Aloe vera* plant extract. Hence, the addition of *Aloe vera* plant extract during the preparation procedure enhances the catalytic properties of $Co_xZn_{1-x}Al_2O_4$.

Acknowledgment: One of the authors, A. Manikandan is thankful to CSIR, New Delhi, India, for the award of Senior Research Fellowship (CSIR-SRF).

References and Notes

1. K. Ariga, T. Mori, and J. P. Hill, *Adv. Mater.* 24, 158 (**2012**).
2. M. Davis, C. Gumeci, R. Alsup, C. Korzeniewski, and L. J. H. Weeks, *Mater. Lett.* 73, 139 (**2012**).
3. Q. He, C. Huang, Z. Wu, and J. Zhang, *Nanosci. Nanotechnol. Lett.* 4, 585 (**2012**).
4. Y. Koseoglu, *Ceram. Int.* 39, 4221 (**2013**).
5. J. Song, M. Leng, X. Fu, and J. Liu, *J. Alloys Compd.* 543, 142 (**2012**).
6. M. Zawadzki, *Solid State Sci.* 8, 14 (**2006**).
7. F. Davar and M. S. Niasari, *J. Alloys Compd.* 509, 2487 (**2011**).
8. Y. Wang, Q. Liao, H. Lei, X. P. Zhang, X. C. Ai, J. P. Zhang, and K. Wu, *Adv. Mater.* 18, 943 (**2006**).
9. S. Farhadi and S. Panahandehjoo, *Appl. Catal. A* 382, 293 (**2010**).
10. R. K. Sharma and R. Ghose, *Ceram. Int.* 40, 3209 (**2014**).
11. X. Y. Chen, C. Ma, Z. J. Zhang, and B. N. Wang, *Mater. Sci. Eng. B* 151, 224 (**2008**).
12. L. Gama, M. A. Ribeiro, B. S. Barros, R. H. A. Kiminami, I. T. Weber, and A. C. F. M. Costa, *J. Alloys Compd.* 483, 453 (**2009**).
13. Y. Wang and K. Wu, *J. Am. Chem. Soc.* 127, 9686 (**2005**).
14. W. Walerczyk, M. Zawadzki, and H. Grabowska, *Catal. Lett.* 141, 592 (**2011**).
15. S. F. Wang, F. Gu, M. K. Lu, X. F. Cheng, W. G. Zou, G. J. Zhou, S. M. Wang, and Y. Y. Zhou, *J. Alloys Compd.* 394, 255 (**2005**).
16. H. J. Fan, M. Knez, R. Scholz, K. Nielsch, E. Pippel, D. Hesse, M. Zacharias, and U. Gosele, *Nat. Mater.* 5, 627 (**2006**).
17. Z. Gu, *Nanosci. Nanotechnol. Lett.* 5, 363 (**2013**).
18. Y. Koseoglu, *Ceram. Int.* 40, 4673 (**2014**).
19. V. G. Bairi, S. E. Bourdo, U. B. Nasini, S. K. Ramasahayam, F. Watanabe, B. C. Berry, and T. Viswanathan, *Sci. Adv. Mater.* 5, 1275 (**2013**).
20. A. S. Prakash, A. M. A. Khasar, K. C. Patil, and M. S. Hegde, *J. Mater. Synth. Process.* 10, 135 (**2002**).
21. S. Choi and M. H. Chung, *Sem. Integrated Med.* 1, 53 (**2003**).
22. S. P. Chandran, M. Chaudhary, R. Pasricha, A. Ahmad, and M. Sastry, *Biotechnol. Prog.* 22, 577 (**2006**).
23. S. Phumying, S. Labuayai, E. Swatsitang, V. Amornkitbamrung, and S. Maensiri, *Mater. Res. Bull.* 48, 2060 (**2013**).
24. S. Maensiri, P. Laokul, J. Klinkaewnarong, S. Phokha, V. Promarak, and S. Seraphin, *Optoelect. Adv. Mater. Rabid Commun.* 2, 161 (**2008**).
25. P. Laokul and S. Maensiri, *J. Optoelect. Adv. Mater.* 11, 857 (**2009**).
26. J. P. Jacobs, A. Maltha, J. G. H. Reintjes, J. Drimal, V. Ponec, and H. H. Brongersma, *J. Catal.* 147, 294 (**1994**).
27. H. Grabowska, W. Mista, J. Trawczynski, J. Wrzyszcz, and M. Zawadzki, *Res. Chem. Intermed.* 27, 305 (**2001**).
28. H. Grabowska, M. Zawadzki, and L. Syper, *Appl. Catal. A: Gen.* 314, 226 (**2006**).
29. H. Grabowska, M. Zawadzki, and L. Syper, *Lett.* 121, 103 (**2008**).
30. H. Grabowska, W. Mista, J. Trawczynski, J. Wrzyszcz, and M. Zawadzki, *Appl. Catal. A: Gen.* 220, 207 (**2001**).
31. W. Mista, M. Zawadzki, and H. Grabowska, *Res. Chem. Intermed.* 29, 137 (**2003**).
32. S. D. Kapse, F. C. Raghuwanshi, V. D. Kapse, and D. R. Patil, *Cur. App. Phys.* 12, 307 (**2012**).
33. F. M. Stringhini, E. L. Foletto, D. Sallet, D. A. Bertuol, O. C. Filho, and C. A. O. Nascimento, *J. Alloys Compd.* 588, 305 (**2014**).
34. R. Ianos, R. Lazau, I. Lazau, and C. Pacurariu, *J. Eur. Ceram. Soc.* 32, 1605 (**2012**).
35. X. Wei and D. Chen, *Mater. Lett.* 60, 823 (**2006**).
36. X. Duan, D. Yuan, and F. Yu, *Inorg. Chem.* 50, 5460 (**2011**).
37. M. Ardit, G. Cruciani, and M. Dondi, *Am. Mineral.* 97, 1394 (**2012**).
38. D. Varshney and K. Verma, *Mat. Chem. Phys.* 140, 412 (**2013**).
39. K. Verma, A. Kumar, and D. Varshney, *Curr. Appl. Phys.* 13, 467 (**2013**).
40. J. Popovic, E. Tkalcec, B. Grzeta, S. Kurajica, and B. Rakvin, *Am. Mineral.* 94, 771 (**2009**).
41. A. F. Osorio, E. P. Villanueva, and J. C. Fernandez, *Mater. Res. Bull.* 47, 445 (**2012**).
42. H. Bai, Z. Liu, and D. D. Sun, *Int. J. Hydrogen Energy* 37, 13998 (**2012**).
43. E. M. A. Jamal, D. Sakthi Kumar, and M. R. Anantharaman, *Bull. Mater. Sci.* 34, 251 (**2011**).

44. L. C. Ming, F. L. Mei, Z. X. Tao, and Z. W. Lie, *Chin. Phys. B* 16, 95 **(2007)**.

45. A. S. Ahmed, S. M. Muhamed, M. L. Singk, S. Tabassum, A. H. Naqvi, and A. Azam, *J. Lumin.* 131, 1 **(2011)**.

46. T. Schmidt, K. Lischka, and W. Zulehner, *Phys. Rev. B* 45, 8989 **(1992)**.

47. B. C. Cheng, S. C. Qu, H. Y. Zhou, and Z. G. Wang, *Nanotechnol.* 17, 2982 **(2006)**.

48. R. Bhargava, P. K. Sharma, R. K. Dutta, S. Kumar, A. C. Pandey, and N. Kumar, Mater. *Chem. Phys.* 120, 393 **(2010)**.

49. D. P. Norton, M. E. Overberg, S. J. Pearton, and K. Pruessner, *Appl. Phys. Lett.* 83, 5488 **(2003)**.

50. J. H. Park, M. G. Kim, H. M. Jang, and S. Ryu, *Appl. Phys. Lett.* 84, 1338 **(2004)**.

51. Y. Koseoglu, Y. C. Durmaz, and R. Yilgin, *Ceram. Int.* 40, 10685 **(2014)**.

52. S. Vaidya, A. Kar, A. Patra, and A. K. Ganguli, *Rev. Nanosci. Nanotechnol.* 2, 106 **(2013)**.

53. A. Kleinauskas, J. K. Kim, G. H. Choi, H. T. Kim, K. Roe, and P. Juzenas, *Rev. Nanosci. Nanotechnol.* 1, 271 **(2012)**.

54. B. K. Pandey, A. K. Shahi, R. K. Swarnkar, and R. Gopal, *Sci. Adv. Mater.* 4, 537 **(2012)**.

55. M. K. Singh, A. Agarwal, R. K. Swarnkar, R. Gopal, and R. K. Kotnala, *Sci. Adv. Mater.* 4, 532 **(2012)**.

56. Q. He, J. Liu, and R. Hu, *Nanosci. Nanotechnol. Lett.* 5, 995 **(2013)**.

57. X. Bai, T. Cao, and C. Cao, *Sci. Adv. Mater.* 4, 1007 **(2012)**.

58. L. S. Silva, S. Gil, N. Gutiérrez, A. Romero, and J. L. Valverde, *Sci. Adv. Mater.* 5, 1907 **(2013)**.

59. A. Manikandan, R. Sridhar, S. A. Antony, S. Ramakrishna, M. Bououdina, and G. Sekaran, *Ceram. Int.* **(2014)**, DOI 10.1016/j.ceramint.2014.06.056.

60. C. G. Ramankutty and S. Sugunan, *Appl. Catal. A* 218, 39 **(2001)**.

61. A. S. Albuquerque, M. V. Tolentino, J. D. Ardisson, F. C. Moura, R. Mendonca, and W. A. Macedo, *Ceram. Int.* 38, 2225 **(2012)**.

62. A. Manikandan, R. Sridhar, S. A. Antony, C. Meganathan, S. Ramakrishna, M. Bououdina, and G. Sekaran, *Ceram. Int.* **(2014)**, DOI 10.1016/j.ceramint.2014.05.122.

63. M. J. Beier, T. W. Hansen, and J. D. Grunwaldt, *J. Catal.* 266, 320 **(2009)**.

64. S. R. Ali, P. Chandra, M. Latwal, S. K. Jain, V. K. Bansal, and S. P. Singh, *Chin. J. Catal.* 32, 1844 **(2011)**.

65. U. R. Pillai and E. Sahle-Demessie, *App. Catal. A: Gen.* 276, 139 **(2004)**.

66. M. D. Boudreau and F. A. Beland, *J. Environ. Sci. Health Part C* 24, 103 **(2006)**.

Received: 7 September 2014. Accepted: 30 September 2014.